Supporting Information

A High-Performance Wearable Thermoelectric Device with Epoxy Resin/ PA/ AlN Composite Heat Sink

*Zheng Zhu, Zhanglong Xia, Yue Hou, * Wei Cao, Xiaolong Sun, Chang Li, Qianfeng Ding, Wenjie Zhou, Ziyan Jiang, Han Tang, Lai Wei, Cheng Lei,* Ziyu Wang,**

The Institute of Technological Sciences, Wuhan University, Wuhan 430072, China
School of Power and Mechanical Engineering, Wuhan University, Wuhan 430072, China.

Corresponding Authors

***Yue Hou - The Institute of Technological Sciences, Wuhan University, Wuhan 430072, China; E-mail: yuehou@whu.edu.cn**

***Cheng Lei - The Institute of Technological Sciences, Wuhan University, Wuhan 430072, China; E-mail: leicheng@whu.edu.cn**

***Ziyu Wang - The Institute of Technological Sciences, Wuhan University, Wuhan 430072, China; E-mail: zywang@whu.edu.cn**

Boundary conditions

In this research, some reasonable assumptions are introduced. On the one hand, it's to exclude other factors that have less influence on the results; on the other hand, it aims to avoid complicating the analysis by studying several factors simultaneously.

Cooling simulation:

1. Thermoelectric devices exchange heat with the air, and the optimized fin-shaped ones also exchange heat with the air.
2. The ambient temperature is 298.15K.
3. Other boundaries are thermally insulated.

Power generation simulation:

1. Thermoelectric devices exchange heat with the air, and the optimized fin-shaped ones also exchange heat with the air.
2. The ambient temperature is 298.15K.
3. Other boundaries are thermally insulated.
4. The temperature of the hot end is set to a constant 298.15K.

WTED preparation process

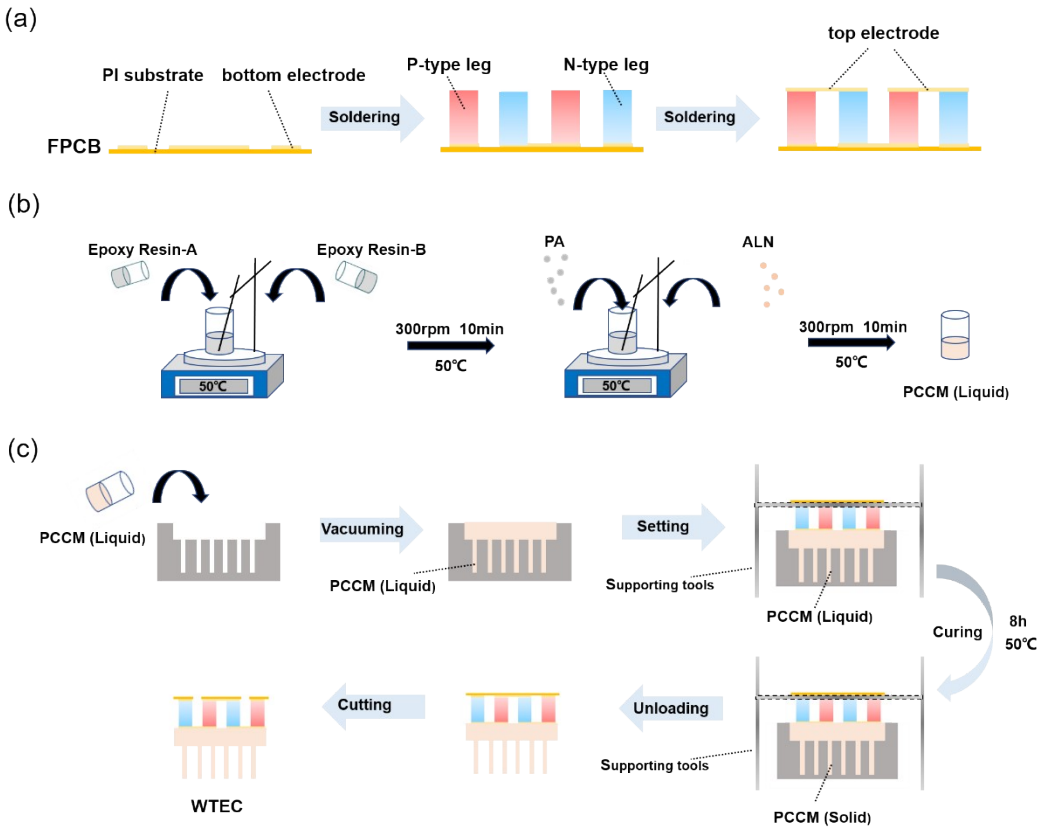

Figure S1 Process flow for the preparation of WTED

Figure S1 illustrates the process flow for the preparation of WTED, which mainly consists of thermoelectric part, liquid phase change heat sink part and curing part.

This paper conducted a refined simulation study on the dimensional parameters of the heat sink fins. First, with the height fixed at 9 mm, the influence of diameter in the range of 1.3 mm to 1.7 mm was examined. Second, with the diameter fixed at 1.5 mm, the effect of height in the range of 3 mm to 11 mm was investigated. Unlike previous simulations, this study specifically coupled the convective heat transfer field, and the convective boundary conditions were applied only to the fin surfaces to more accurately capture the dimensional effects. As shown in Supplementary Fig. S2a, at a temperature difference of 30 K, the output voltage gradually increases with diameter: 1.598 mV at 1.3 mm, 1.758 mV at 1.5 mm, and 1.881 mV at 1.7 mm. This indicates that increasing the diameter benefits heat dissipation performance.

$$Gr = \frac{g\beta(T_s - T_\infty)D^3}{v^2} \quad (1)$$

$$Ra = Gr \cdot Pr \quad (2)$$

Where g is gravitational acceleration, β is the thermal expansion coefficient of air, T_s is the fin surface temperature, T_∞ is the ambient temperature, D is the fin diameter, v is the kinematic viscosity of air, and Pr is the Prandtl number. Based on the Churchill–Chu correlation, the Nusselt number (Nu) is expressed as:

$$Nu = \left[0.6 + 0.387Ra^{1/6}\left(1 + \left(\frac{0.559}{Pr}\right)^{9/16}\right)^{-8/27}\right]^2 \quad (3)$$

The convective heat transfer coefficient (h) is then:

$$h = \frac{Nu \cdot k_{air}}{D} \quad (4)$$

where k_{air} is the thermal conductivity of air. It can be seen that $h \propto D^{-0.5}$. Therefore, the total heat dissipation Q for a single cylindrical fin is:

$$Q = h \cdot A \cdot \Delta T \tag{5}$$

For a single cylinder, the surface area $A = \pi DL$, where L is the height of fin. Hence, $Q \propto D^{0.5}$, indicating that increasing the fin diameter enhances heat dissipation performance[40]. From the heat balance equation:

$$mc_p \frac{dT}{dt} = Q_{in} - hA(T_s - T_\infty) \tag{6}$$

$$\frac{dT}{dt} = \frac{Q_{in}}{mc_p} - \frac{4h(T_s - T_\infty)}{\rho D c_p} \tag{7}$$

Where $m = \rho V$ is the mass, Q_{in} is the external input power, ρ is the density, and the volume $V = \pi(0.5D)^2 L$. Both mass m and surface area A grow linearly with height L. Under natural convection conditions, when Q_{in} is small, the term $4(T_s - T_\infty)/\rho D c_p$ dominates, so the influence of L is minimal. Therefore, even if the fin height increases, the change in heat dissipation effect is not significant[40], which is consistent with the simulation results.

Experimentally, under ambient conditions of 22 °C and an applied source temperature of 31 °C, we compared the thermoelectric power generation of deformed and non-deformed fins. As shown in Fig. S2c, d, the deformed fin could not light the LED, while the non-deformed fin could, directly demonstrating that deformation-induced contact affects device performance.

Integrating the above results, we further optimized the fin dimensions: as shown in Fig. S2a, an excessively large diameter increases the risk of deformation-induced contact; as shown in Fig. S2b, performance improved by 0.40 % when height increased

from 5 mm to 7 mm, by 0.74 % from 7 mm to 9 mm, but only by 0.07 % from 9 mm to 11 mm, indicating a clear inflection point around 9 mm. From a manufacturing perspective, a diameter that is too small can lead to insufficient filling and structural fragility, and such fins are prone to breakage during demolding. Moreover, when the aspect ratio exceeds 6.7, the fins are susceptible to warping or damage. Therefore, we ultimately selected a fin diameter of 1.5 mm and a height of 9 mm, achieving a balance among heat dissipation performance, deformation resistance, and dimensional compactness.

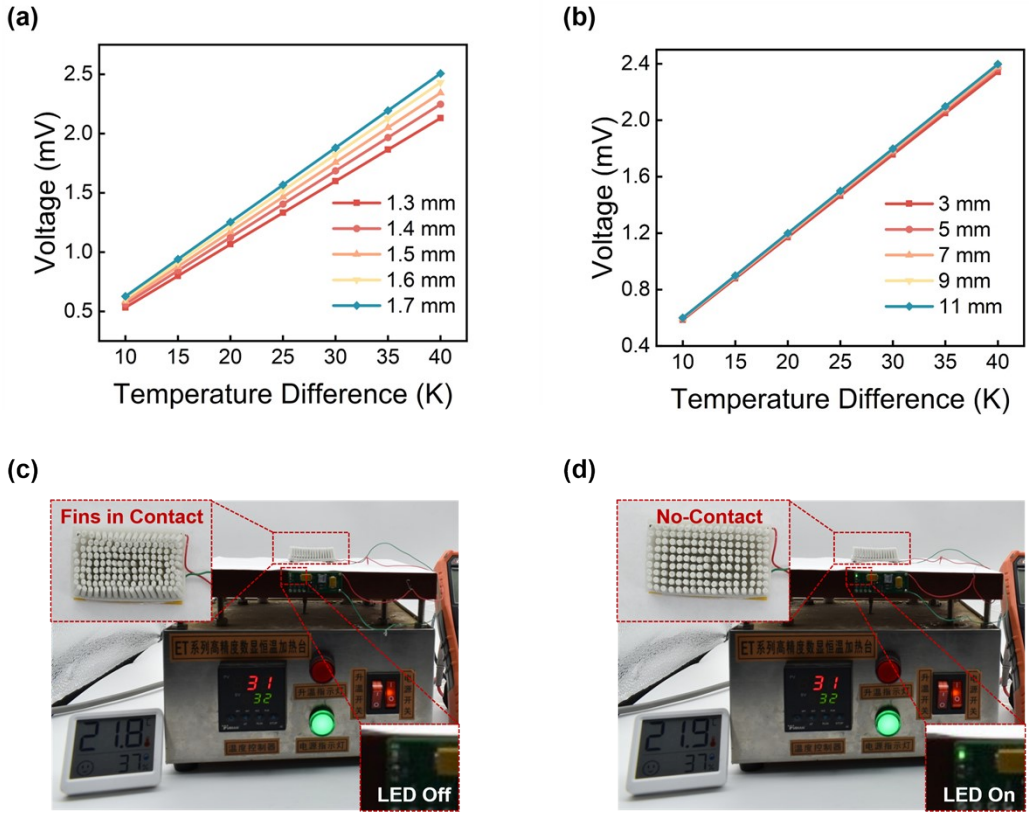

Figure S2 Geometry design of heat dissipation fins. a) Simulated thermoelectric output voltage curves for different fin diameters. b) Simulated thermoelectric output voltage curves for different fin heights. c) Deformed heat dissipation fins failed to light up the LED. d) Undeformed heat dissipation fins successfully lit up the LED.

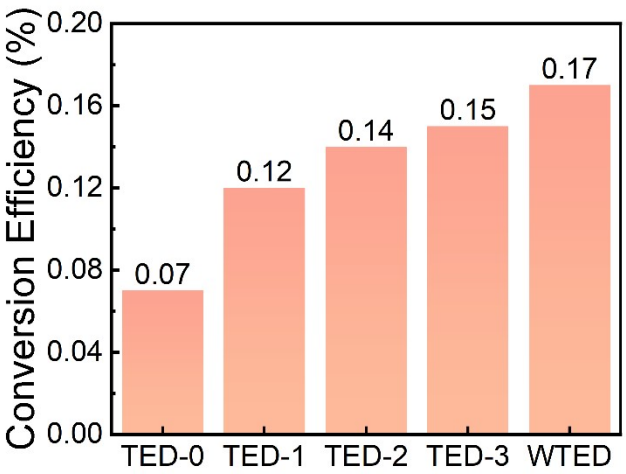

Figure S3 The thermoelectric conversion efficiency from TED-0 to WTED after optimization.

The thermoelectric conversion efficiency from TED-0 to WTED was simulated, as shown in Fig. S3. Without any heat dissipation measures, the conversion efficiency of TED-0 was 0.07%. Upon incorporating a PA-based heat sink, the efficiency increased to 0.12%. Further enhancement was achieved by removing the PI layer of the TED to reduce interfacial thermal resistance, resulting in an efficiency of 0.14% for TED-2. Building upon TED-2, the efficiency was further improved to 0.15% by expanding the heat dissipation area through a fin-like structure. Finally, with the addition of highly thermally conductive AlN, the conversion efficiency of WTED reached 0.17%, representing a 143% improvement over TED-0 and further validating the effectiveness of the proposed optimization strategy.

This paper proposes a performance optimization scheme for TEDs, as shown in Fig. 2. This scheme significantly improves power generation performance and cooling effects through structural improvements to conventional TEDs.

First, the impact of device optimization on power generation performance is explored. Based on previous research, the temperature difference across the TE leg is proportional to the TE output voltage and also proportional to the temperature difference across the TED:

$$\Delta T_{leg} = T_h - T_c = \frac{R}{R + R_{HS} + R_{PI}} \cdot (T_h^{'} - T_c^{'}) \quad (1)$$

A steady-state heat balance equation for the cold end is established as follows, with the hot end temperature held constant:

$$\left(T_h^{'} - T_c^{'}\right) K_3 = h_c^{'} S (T_c^{'} - T_{air}) \quad (2)$$

Transformed into:

$$T_c^{'} = \frac{K_3 T_h^{'} + h_c^{'} S T_{air}}{h_c^{'} S + K_3} = T_{air} + \frac{K_3 (T_h^{'} - T_{air})}{h_c^{'} S + K_3} \quad (3)$$

Where, T_h and T_c are the temperatures at the hot and cold ends of the TE leg, respectively; R, R_{HS} and R_{PI} are the thermal resistances of the TE leg, heat sink, and PI layer, respectively; $T_h^{'}$ and $T_c^{'}$ are the temperatures at the hot and cold ends of the TED, respectively. K_3represents the effective thermal conductance of the TED, $h_c^{'}$ is the heat transfer coefficient at the cold end of the TED, S is the contact surface area for heat exchange with air, and T_{air} is the air temperature.

Simulation results indicate that the conventional TED-0 without a heat sink (Fig. 2a, b) achieved lower power generation performance, with an output voltage of only 0.94 mV at a temperature difference of 30 K. Therefore, a heat sink was introduced in TED-1 to enhance convective heat dissipation at the cold end. According to Formula 3, an increase in $h_c^{'}$ leads to a decrease in $T_c^{'}$, which in turn increases $T_h^{'} - T_c^{'}$, thus increasing the output voltage. However, in TED-1, the separate design between the thermoelectric module and the heat sink introduced significant interfacial thermal resistance, reducing heat transfer efficiency and impairing the TED's output performance. To address this issue, in TED-2, the PI encapsulation layer between the thermoelectric unit and the heat sink was removed, integrating the thermoelectric unit and the heat sink into a monolithic structure. This integration reduced the interfacial thermal resistance. According to Formula 1, $R_{PI} = 0$, thus ΔT_{leg} increases, leading to an increased output voltage. Furthermore, in TED-3, the heat sink was fabricated into a finned structure, expanding the heat dissipation area. According to Formula 3, an increase in S leads to a decrease in $T_c^{'}$, thus increasing the output voltage. Finally, by incorporating high thermal conductivity AlN into the heat sink, the output voltage was further increased. According to Formula 3, $h_c^{'}$increases further, enhancing the thermoelectric output performance of the WTED (output voltage of 1.42 mV at a 30 K temperature difference), representing a 50% improvement compared to TED-0.

Next, the impact of device optimization on the cooling effect was explored. First, the heat balance equation for the hot end of the TED (position 2 in Fig. S4) was established:

$$K_2\left(T_h - T_h^{'}\right) = h_2 S(T_h^{'} - T_{air}) \quad (4)$$

Transformed into:

$$T_h^{'} = \frac{-h_2 S T_{air} - K_2 T_h}{-K_2 - h_2 S} = T_{air} + \frac{K_2 T_{air} - K_2 T_h}{-K_2 - h_2 S} \quad (5)$$

Where K_2 is the effective thermal conductance of the PCM and PI, and h_2 is the heat transfer coefficient between the hot end and the air. Simulation results show that TED-0, which lacks a heat sink, only achieved a temperature drop of 3.48°C. TED-1 added a heat sink to TED-0, causing h_2 to increase, which led to a decrease in $T_h^{'}$. Furthermore, the heat balance equation for the hot end of the thermoelectric leg (position 1 in Fig. S4) was established:

$$\alpha I T_h - K_1\left(T_h - T_c\right) - K_2\left(T_h - T_h^{'}\right) + 0.5 I^2 R = 0 \quad (6)$$

Transformed into:

$$T_h = \frac{K_1 T_c + 0.5 I^2 R + K_2 T_h^{'}}{K_1 + K_2 - \alpha I} \quad (7)$$

Where K_1 is the effective thermal conductance of the TE leg. From Formula 7, it can be seen that a decrease in $T_h^{'}$ leads to a decrease in T_h. Additionally, the heat balance equation at the cold end position (position 3 in Fig. S4) is established:

$$K_1\left(T_h - T_c\right) + K_2\left(T_c^{'} - T_c\right) + 0.5 I^2 R = \alpha I T_c \quad (8)$$

Transformed into:

$$T_c = \frac{K_1 T_h + 0.5 I^2 R + K_2 T_c^{'}}{K_1 + K_2 + \alpha I} \quad (9)$$

According to Formula 9, a decrease in T_h leads to a decrease in T_c. Assuming the cold end heat transfer conditions remain unchanged, this leads to a decrease in $T_c^{'}$. Therefore, the cooling performance of TED-1 is improved compared to TED-0.

TED-2 removed the PI layer compared to TED-1, resulting in an increase in K_2. Transforming Formula 5:

$$T_h^{'} = T_h - \frac{h_2 S T_h - h_2 S T_{air}}{K_2 + h_2 S} \quad (10)$$

According to Formula 10, an increase in K_2 leads to an increase in $T_h^{'}$. Combining Formulas 4 and 6 yields:

$$T_h = \frac{-0.5 I^2 R - K_1 T_c - h_2 S T_h^{'} + h_2 S T_{air}}{\alpha I - K_1} = T_c - \frac{-0.5 I^2 R - \alpha I T_c - h_2 S T_h^{'} + h_2 S T_{air}}{K_1 - \alpha I}$$

(11)

It can be seen that an increase in $T_h^{'}$ leads to a decrease in T_h. Following the same subsequent steps as the improvement from TED-0 to TED-1, it is similarly concluded that $T_c^{'}$ decreases.

TED-3, based on TED-2, fabricated the heat sink into a finned shape, increasing the heat dissipation area. According to Formula 5, an increase in S causes $T_h^{'}$ to decrease and, as described above, also leads to a decrease in $T_c^{'}$. The final WTED incorporated high thermal conductivity AlN into TED-3. As in the first step, K_2 increases further, leading to a decrease in $T_c^{'}$. The final simulation achieved a temperature drop of 5.77°C, which is 2.29 degrees Celsius lower than TED-0's temperature, representing a 66% improvement in cooling effect.

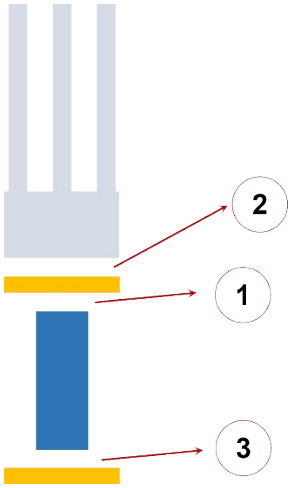

Figure S4 Layered schematic diagram of the TED.

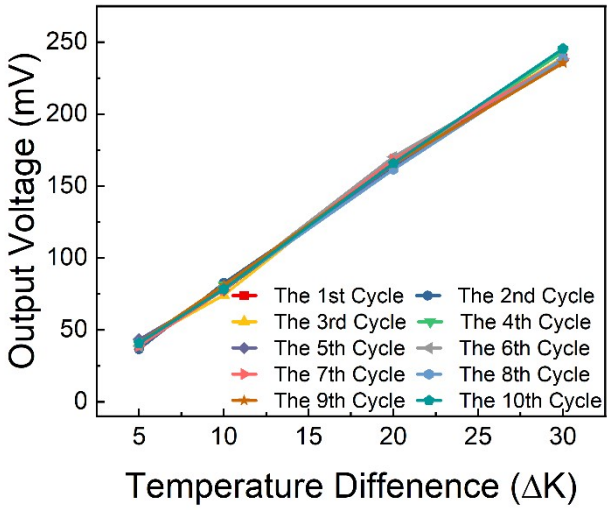

Figure S5 Output voltage of the WTED over 10 thermal cycles under different ΔT.

The operational stability of the proposed wearable thermoelectric device (WTED) was evaluated through ten consecutive thermal cycles, with its output voltage recorded across a temperature difference (ΔT) range of 5 K to 30 K. As shown in Figure S5, the device exhibits a highly consistent voltage output throughout all cycles, with the curves showing close alignment across the entire temperature range. These results confirm the excellent repeatability and thermal cycling stability of the WTED, highlighting its reliability for long-term wearable applications.

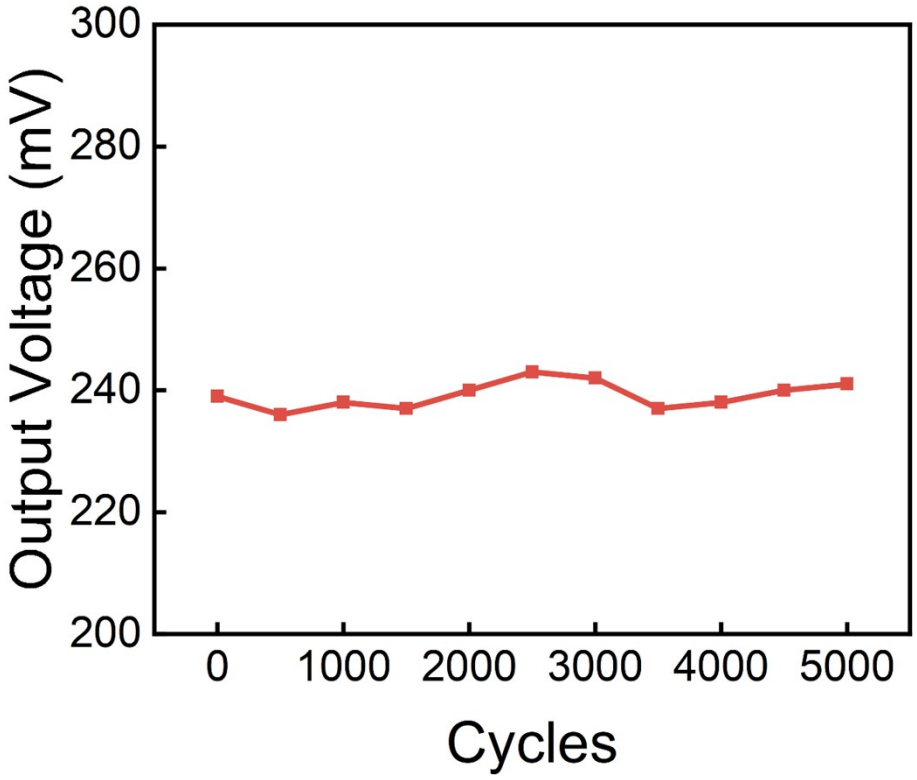

Figure S6 The thermoelectric output voltage after 5000 bending cycles.

The WTED was palsed on a flexible tester, simulating the bending radius shown in Fig. 4f, and conducted 5000 cyclic bending tests, recording the thermoelectric output voltage every 500 cycles. As shown in Fig. S6, despite periodic contact and separation of the fins during repeated bending, the output voltage consistently remained within the error range, demonstrating good cyclic stability and reliability.

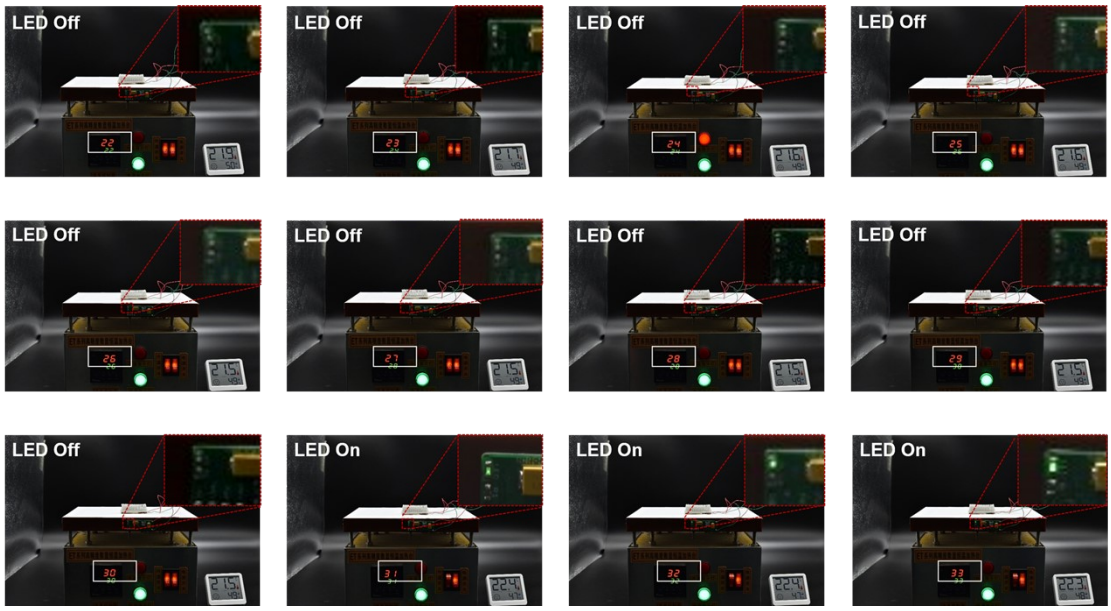

Figure S7 Temperature-dependent LED lighting performance of WTED under gradient temperatures (22-33 °C) at ambient temperature ~21.7 °C.

Figure S5 illustrates the temperature-dependent LED lighting performance of the WTED across a temperature gradient from 22 °C to 33 °C under an ambient temperature of approximately 21.7 °C. As shown, the LED remains off when the applied temperature is below 31 °C (from 22 °C to 30 °C). Once the temperature reaches 31 °C, the LED is successfully lit and maintains illumination at higher temperatures (31-33 °C), demonstrating that 31 °C is the minimum temperature required for the WTED to drive LED lighting.